Experimental characterization of hot-electron emission and shock dynamics in the context of the shock ignition approach to inertial confinement fusion

A. Tentori, A. Colaitis, W. Theobald, A. Casner, D. Raffestin, A. Ruocco, J. Trela, E. Le Bel, K. Anderson, M. Wei, B. Henderson, J. Peebles, R. Scott, S. Baton, S. A. Pikuz, R. Betti, M. Khan, N. Woolsey, S. Zhang, and D. Batani

Published version information

Citation: A Tentori et al. Experimental characterization of hot-electron emission and shock dynamics in the context of the shock ignition approach to inertial confinement fusion. Phys Plasmas 28, no. 10 (2021): 103302

DOI: 10.1063/5.0059651

Physics of Plasmas

Experimental characterization of hot-electron emission and shock dynamics in the context of the shock ignition approach to inertial confinement fusion

Cite as: Phys. Plasmas **28**, 103302 (2021); https://doi.org/10.1063/5.0059651
Submitted: 10 June 2021 • Accepted: 13 September 2021 • Published Online: 12 October 2021

A. Tentori, A. Colaitis, W. Theobald, et al.

Physics of Plasmas ARTICLE scitation.org/journal/php

Experimental characterization of hot-electron emission and shock dynamics in the context of the shock ignition approach to inertial confinement fusion

Cite as: Phys. Plasmas **28**, 103302 (2021); doi: 10.1063/5.0059651
Submitted: 10 June 2021 · Accepted: 13 September 2021 ·
Published Online: 12 October 2021

A. Tentori,[1,a)] A. Colaitis,[1] W. Theobald,[2,3] A. Casner,[1] D. Raffestin,[1] A. Ruocco,[1,4] J. Trela,[1] E. Le Bel,[1] K. Anderson,[2] M. Wei,[2] B. Henderson,[2] J. Peebles,[2] R. Scott,[4] S. Baton,[5] S. A. Pikuz,[6] R. Betti,[2,3,7] M. Khan,[8] N. Woolsey,[8] S. Zhang,[9] and D. Batani[1]

AFFILIATIONS

[1]Centre Lasers Intenses et Applications, CELIA, Université Bordeaux CEA-CNRS, UMR 5107, F-33405 Talence, France
[2]Laboratory for Laser Energetics, University of Rochester, Rochester, New York 14623, USA
[3]Department of Mechanical Engineering, University of Rochester, Rochester, New York 14623, USA
[4]Central Laser Facility, STFC Rutherford Appleton Laboratory, Harwell Oxford, Didcot, Oxford OX11 0QX, United Kingdom
[5]Laboratoire pour l'Utilisation des Lasers Intenses, LULI, CNRS-Ecole Polytechnique-CEA-Sorbonne Universités, UMR 7605, F-91128 Palaiseau, France
[6]Joint Institute for High Temperatures of Russian Academy of Sciences, 125412 Moscow, Russian Federation
[7]Department of Physics and Astronomy, University of Rochester, Rochester, New York 14623, USA
[8]Department of Physics, York Plasma Institute, University of York, Heslington, York YO10-5DD, United Kingdom
[9]Center for Energy Research, University of California San Diego, La Jolla, California 92093, USA

[a)]**Author to whom correspondence should be addressed:** alessandro.tentori@u-bordeaux.fr and alessandro.tentori@mail.polimi.it

ABSTRACT

We report on planar target experiments conducted on the OMEGA-EP laser facility performed in the context of the shock ignition (SI) approach to inertial confinement fusion. The experiment aimed at characterizing the propagation of strong shock in matter and the generation of hot electrons (HEs), with laser parameters relevant to SI (1-ns UV laser beams with I $\sim 10^{16}$ W/cm^2). Time-resolved radiographs of the propagating shock front were performed in order to study the hydrodynamic evolution. The hot-electron source was characterized in terms of Maxwellian temperature, T_h, and laser to hot-electron energy conversion efficiency η using data from different x-ray spectrometers. The post-processing of these data gives a range of the possible values for T_h and η [i.e., T_h[keV] $\in$ (20, 50) and $\eta \in$ (2%, 13%)]. These values are used as input in hydrodynamic simulations to reproduce the results obtained in radiographs, thus constraining the range for the HE measurements. According to this procedure, we found that the laser converts $\sim$10% $\pm$ 4% of energy into hot electrons with $T_h = 27 \pm 8$ keV. The paper shows how the coupling of different diagnostics and numerical tools is required to sufficiently constrain the problem, solving the large ambiguity coming from the post-processing of spectrometers data. The effect of the hot electrons on the shock dynamics is then discussed, showing an increase in the pressure around the shock front. The low temperature found in this experiment without pre-compression laser pulses could be advantageous for the SI scheme, but the high conversion efficiency may lead to an increase in the shell adiabat, with detrimental effects on the implosion.

I. INTRODUCTION

Shock ignition (SI) is an alternative approach to direct-drive inertial confinement fusion that is based on the separation of the compression and the ignition phases. A low-intensity laser pulse of $\sim 10^{14}$ W/cm^2 compresses the fuel, followed by an high-intensity ($\sim 10^{16}$ W/cm^2) "spike." This latter launches a strong converging shock at the end of the compression phase. The collision of this shock with the rebound compression shock raises the hotspot pressure

creating the conditions to ignite the fuel.[1–3] The high laser intensity required in the ignition phase exceeds the thresholds for the generation of different laser-plasma instabilities (LPIs). These instabilities take place in the underdense region of the plasma, preventing part of the laser energy from arriving at the critical surface where more efficient absorption mechanisms can occur. In addition, large amounts of hot electrons are generated by the electron plasma waves (EPWs) created by stimulated Raman scattering (SRS) and two-plasmon decay (TPD).[4,5] These hot electrons (HEs) may preheat the fuel, making the compression more difficult, or they can increase the hotspot mass by ablating the inner shell interface and hence increasing the threshold for ignition.[6,7] On the other hand, an enhanced shock and ablation pressure from low-temperature hot electrons are predicted.[8] In particular, these effects were investigated in planar[9,10] and spherical target configuration[11] experiments. As such, a critical step for assessing the feasibility of shock ignition is the characterization in terms of energy and number of the hot-electron population and to understand its effects on the hydrodynamics of the target. Although several experiments have addressed this point,[12,13] we are still far from a complete comprehension of the problem, especially in conditions that are directly relevant to SI.[14]

In this context, we performed an experiment at the OMEGA-EP laser facility in the intensity range required for shock ignition. A UV ($\lambda = 351$ nm) laser of intensity of $\sim 10^{16}$ W/cm^2 was focused on a planar multilayer target producing a strong shock. Because of the absence of low-intensity pre-compression beams, the plasma scale lengths and the coronal electronic temperatures reached in this experiment ($L_n \sim 150\,\mu$m, $T_e \sim 2$ keV) are lower compared to the real SI conditions ($L_n \sim 600\,\mu$m, $T_e \sim 5$ keV).

The shock propagation was monitored using x-ray time-resolved radiography. Several x-ray spectrometers were used to characterize the hot-electron beam in terms of temperature and intensity, and a backscattering spectrometer was used to collect the laser backscattered light.

The paper is structured as follows: a description of the experimental setup and the diagnostics involved is given in the first part. Then, we describe the post-processing techniques of the spectrometer data and the coupling with hydrodynamic simulations done in order to characterize the electron beam. Finally, we discuss the evolution of hydrodynamic quantities considering the influence of hot electrons.

II. EXPERIMENTAL SETUP

The experiment was performed in the target chamber of the four-beam OMEGA-EP laser facility[15] at the Laboratory for Laser Energetics. One or two high-intensity UV interaction beams (B1, B4) ($\lambda = 351$ nm, 1.0 ns square pulse, beam energy of $\sim$ 1.25 kJ, $f/6.5$) irradiated a multi-layer target to produce a strong shock wave and copious amount of hot electrons. The UV interaction beams were tightly focused on the target surface without phase plates to a focal spot size of $\sim$ 130 μm providing a nominal vacuum laser intensity of $\sim 1 \times 10^{16}$ W/cm^2 for one beam and $\sim 2 \times 10^{16}$ W/cm^2 for two beams. Planar targets consisted of two layers (175 or 250 μm CH/20 or 10 μm Cu) fabricated to 500 μm diameter disks. These were mounted on a 50 μm thick CH slab aiming at inhibiting hot-electron recirculation. The UV interaction lasers impinged on front of the 175 (or 250) μm thick CH layer at an angle of incidence of 23° with respect to the target normal. The Cu middle layer served as a tracer for hot electrons emitting Cu K_α x rays of 8.05 keV. Multiple x-ray diagnostics characterized the emission generated by the hot-electron population in order to obtain information on their energy spectrum.

The total yield of Cu K_α was measured by an absolutely calibrated Zinc von Hamos x-ray spectrometer (ZnVH).[16] This spectrometer uses a curved HOPG crystal in von Hamos geometry to diagnose the x-ray spectrum in the range of $7 - 10$ keV. A high-spectral resolution x-ray spectrometer (HRS) used a spherically bent Si [220] crystal coupled to a charge-coupled device to measure the time-integrated x-ray emission in the 7.97- to 8.11-keV range.[17] The hot-electron-produced bremsstrahlung radiation was diagnosed by two time-integrating hard x-ray spectrometers (BMXSs)[18] at 25° and 65° off the target rear normal, respectively. The instruments are composed of a stack of fifteen imaging plates (IPs) of MS type,[19] alternated by filters of different metals. The x rays propagate into the stack creating a signal in the IPs according to their energy: higher energy photons propagate deeper in the stack. A schematic view of the filters disposition is shown in Fig. 1.

The whole stack is encapsulated in a cylindrical lead container in order to reduce the background signal, and a further 10 mm filter of polytetrafluoroethylene $(C_2F_4)_n$ (PTFE, Teflon) is placed in front of the stack shielding it from plasma debris. In addition, this filter blocks low-energy photons coming from the coronal plasma and the copper K_α signal, while allowing higher energy photons produced by the propagation of hot electrons in the target.

A streaked sub-aperture backscattering spectrometer (SABS) diagnosed the temporally resolved spectrum of the SRS backscattered light (430 to 750 nm). However, the total SRS reflected power could not be directly measured due to the small collecting area.

One UV beam (B3) with a 3 ns square pulse irradiated a V foil target to produce backlighter with a high flux of x-ray radiation at 5.2 keV, vanadium He_α line, used as source to perform time-resolved radiographs (see Fig. 2). A total energy of $\sim$2.7 kJ impinged on the V foil. The average intensity ranged from 3×10^{14} to 5×10^{14} W/cm^2. A 50 μm thick CH heat shield placed between the backlighter and the target absorbed the soft x-ray radiation from the V foil in order to prevent any premature x-ray preheat of the multi-layer target.

A four-strip x-ray framing camera (XRFC)[20] equipped with an 4×4 array of 20-μm-diameter pinholes captured sixteen 2D images of the shock front with 6× magnification at various times. The time and the spatial resolutions of the camera were $\sim$100 ps and $\sim$15 μm, respectively.

FIG. 1. Schematic disposition of the filters (in gray) and imaging plates (in blue). X rays are penetrating the stack from the right.

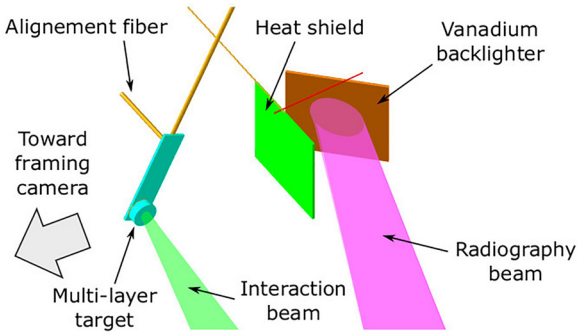

FIG. 2. Experimental setup for x-ray radiography. One UV beam irradiated a V foil and one or two high intensity UV beams interacted with the multi-layer target. An x-ray framing camera equipped with a pinhole array captured images of the shock front at various times.

Finally, 1D time-resolved radiography was obtained by replacing the XRFC with a slit imager and an x-ray streaked camera. The PJX (a high-current, high-dynamic-range x-ray streak camera) streak camera[21] was operated in inverse mode with an 6 mm × 90 μm input slit and 10 × 1000 μm^2 imaging slit providing a total magnification of 20×. The spatial resolution was about 10 μm and 40 ps of temporal resolution.

Table I presents a list of the performed shots considered in this paper, indicating the availability of experimental data from the diagnostics.

III. CHARACTERIZATION OF HOT ELECTRONS

Here, we present the methodology of analysis and post-processing of the BMXS and ZnVH data. The response of the spectrometers is analyzed using Monte Carlo simulations, providing a first estimation of the HE source. The results are then set as input in hydrodynamic simulations to reproduce the experimental behavior observed in the radiography and refine the evaluation of the HE source.

A. Time-integrating hard x-ray spectrometer BMXS

The BMXSs are made by a stack of 15 image plate detectors with metal filters interleaved in-between (see Sec. II). After recording the signal, the imaging plates are read in a dedicated scanner which induces photo stimulated luminescence (PSL). Figure 3 shows the signal recorded in shot No. 28407. In general, all the shots had signal up to the seventh or eighth IP. The background noise is around 1% of the signal of the seventh IP, and it does not influence the measurement. The PSL value is related to the absorbed dose by a calibration curve.[22]

To extract the x-ray spectrum that led to a given energy deposition, one must first characterize the response of each IP inside the BMXS to a monochromatic x-ray beam. This is calculated by performing MC simulations in which the 3D detector geometry is reproduced. The simulations were performed with the Geant4 MC code[23] using the physics library Penelope.[24] Here, we used 46 logarithmically spaced photon spectral bins from 5 keV to 1 MeV in order to calculate the deposited energy per photon $D_i(k)$, in the kth IP for the ith energy bin. The results are shown in Fig. 4.

For a generic photon distribution function $f_{\mathrm{ph}}(E)$, it is possible to calculate the energy deposition E_{t} in the kth IP using the below formula:

$$E_{\mathrm{t}}(k) = \sum_{i=1}^{45} \int_{E_i}^{E_{i+1}} f_{\mathrm{ph}}(E) \frac{D_i(k) + D_{i+1}(k)}{2} \mathrm{d}E. \quad (1)$$

Considering the decaying behavior of the signal through the IPs, we chose an exponential photon distribution function of the type $f_{\mathrm{ph}}(A_{\mathrm{ph}}, T_{\mathrm{ph}}, E) = \frac{A_{\mathrm{ph}}}{E} e^{-E/T_{\mathrm{ph}}}$ with free parameters A_{ph} and T_{ph}. The choice of this type of $f_{\mathrm{ph}}(E)$ is related to the fact that, as remarked later, this is the shape of photon distribution function produced on the detector by a 2D electron Maxwellian distribution function that propagates inside the target. Furthermore, theoretical studies predict that this kind of curves corresponds to the photon distribution function produced by a 3D electron Maxwellian that propagate in an infinite homogeneous plasma.[25] The values of the free parameters A_{ph} and

TABLE I. Summary of performed shots. Shot number and the correspondent interaction laser beam focused on target are shown. The availability of experimental data coming from x-ray spectrometers and from radiography is indicated. In the radiographies Nos. 28410 and 28415, the poor contrast of the images makes the radiographies not exploitable.

Shot Number	Interaction beam on target	BMXS	ZnVH	Radiography	HRS
28406	B4	Available	Available	2D not available	Available
28407	B1	Available	Available	2D available	Available
28410	B1 + B4	Available	Not available	2D available but not exploitable	Available
28412	B1	Available	Available	1D available	Available
28415	B1 + B4	Available	Available	1D available but not exploitable	Available

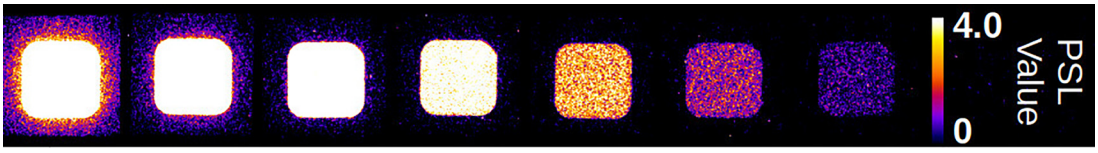

FIG. 3. Example signals obtained in the IP stack for shot No. 28407.

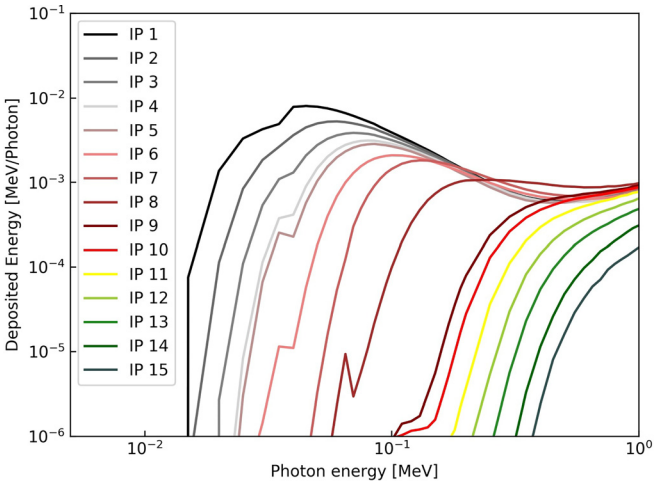

FIG. 4. Response curves of each IP in the BMXS spectrometer calculated using MC simulations.

T_{ph} are found fitting the experimental data by performing a reduced χ^2 test. The latter reads

$$\chi^2 = \frac{1}{\nu}\sum_{k=1}^{N_{ip}} \frac{\left(E_t(k) - E_{exp}(k)\right)^2}{\sigma^2_{exp}(k)} \to 1, \quad (2)$$

where $E_t(k)$ is the calculated deposited energy, $E_{exp}(k)$ is the experimental one, σ^2_{exp} is the variance of the experimental value, and ν is the number of degrees of freedom.

Figure 5 shows the ensemble of the possible values for the parameters A_{ph} and T_{ph} that lead to $\chi^2 \to 1$ for the two spectrometers, for shot No. 28407. In general, a good agreement between the two spectrometers was observed for all shots.

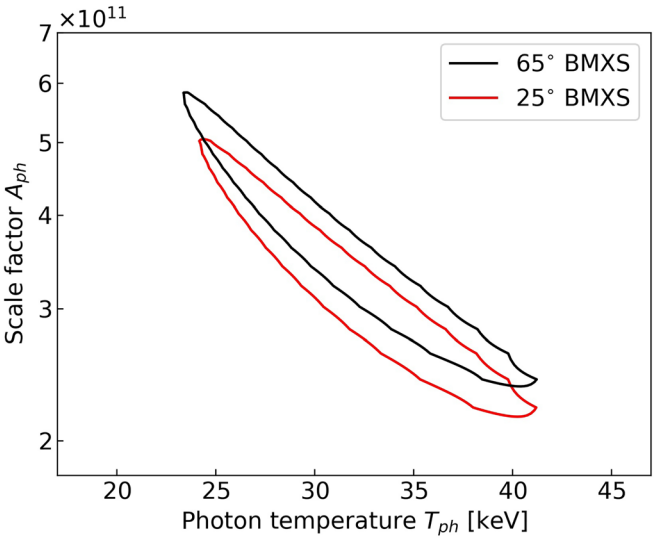

FIG. 5. Contours of parameters A_{ph} and T_{ph} leading to a reduced χ^2 of 1 in the post-processing of data from the two BMXS, for shot No. 28407. The results for the spectrometers placed at 25° and 65° are given in red and black, respectively.

Since there are several combinations of the possible values for the parameters A_{ph} and T_{ph} that can reproduce the measurements, in the continuation of our analysis we consider three representative points for each BMXS (see Fig. 6): the two extreme points (f_{ph1} and f_{ph3}) and the central point (f_{ph2}). The proposed method presents a large uncertainty in the determination of the parameters A_{ph} and T_{ph}. Nevertheless, the three obtained curves lead to an energy deposition in the IPs that is consistent with the experimental error of the measure [see Fig. 6(b)]. The error is evaluated considering the standard deviation calculated from the signal in the IPs. The degeneracy of the solutions requires to constrain the problem using other experimental results.

B. K_α spectrometers

The two K_α spectrometers, the ZnVH and the HRS, are based on the same working principle: a crystal disperses the x-ray photons on

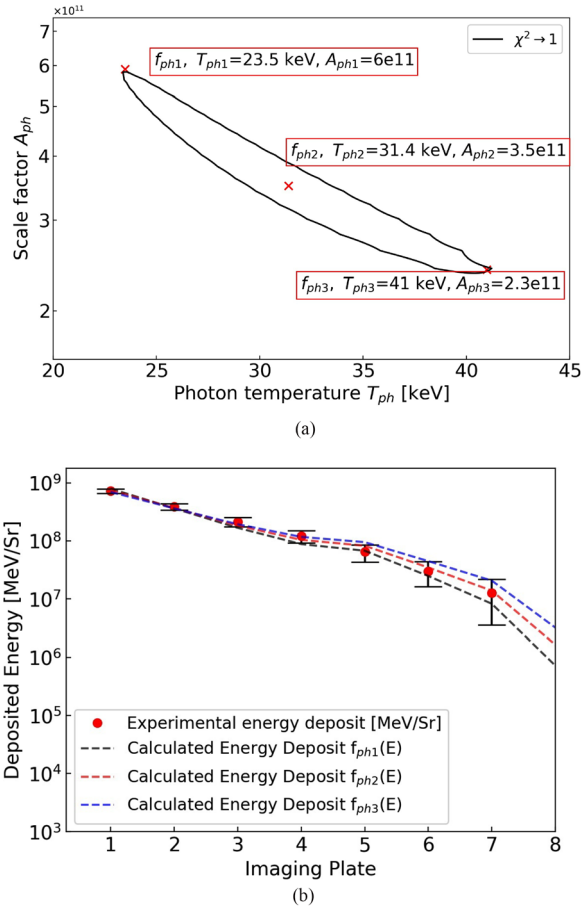

FIG. 6. (a) Contours of parameters A_{ph} and T_{ph} leading to a reduced χ^2 of 1 in the post processing of the BMXS placed at 65° for the shot No. 28407. The three representative points with the corresponding values of A_{ph} and T_{ph} are indicated. (b) Experimental deposited energy in the IPs (red dots) and theoretical energy deposition expected considering the three f_{ph} (dashed lines).

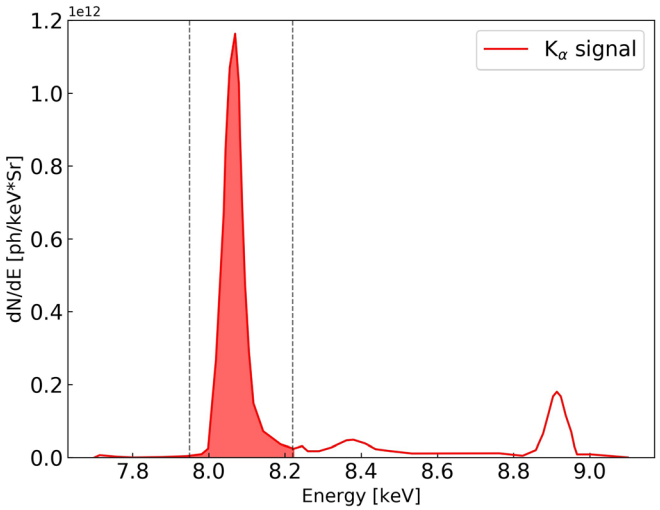

FIG. 7. X-ray spectrum detected by the ZnVH spectrometer for the shot No. 28407, after the background correction.

the sensitive part of the detector. In the ZnVH, a passive detection system is used, the imaging plate, while the HRS uses a CCD. Knowing the calibration of the spectrometers, it is possible to reconstruct the x-ray spectrum detected. Figure 7 shows the signal detected by the ZnVH for the shot No. 28407, after a correction for the background. In the figure, it is possible to appreciate how the Cu K_α peak is well resolved by the diagnostic. The integral of the peak gives the total number of K_α photon per steradian that reached the instrument. As shown by Fig. 8, the two spectrometers gave a consistent response in terms of order of magnitude. As such, in the continuation of our analysis, we will consider only the data from the ZnVH.

C. Post-processing of the BMXS and ZnVH

Information on the hot-electron population is inferred by simulating the propagation of the hot-electron beam in the target and finding the parameters that reproduce both the bremsstrahlung emission and the K_α signal detected by the diagnostics. These simulations are performed with Geant4,[23] which allows for a detailed description of the electron collision in matter and x-ray emission. Unfortunately, the code does not account for the hydrodynamic evolution of the target and the collective effects, but these are playing a minor role in determining the x-ray emission due to electron propagation. For sufficiently large laser spot, the 1D assumption that the product ρr is the same for cold and for ablated target holds, where r is the target length and ρ is the mass density for the two cases. Hence, at first order, electrons should lose a similar amount of energy crossing a cold target or the real irradiated one.

While the geometry and composition of targets are fully described in the simulation, reproducing the exact position and geometry of the detectors would require significant computational resources in order to achieve acceptable statistics. Indeed, the spectrometers were mounted on the chamber wall at 1.8 m from target chamber center (TCC). For these reasons, the detectors in the MC simulation are represented by spherical coronas at the correct angle and distance. This approach improves statistics, but assumes cylindrical symmetry (see Fig. 9).

The electron beam with a size of 100 μm is injected from the front side of the target where the laser impinges. Various cases are considered concerning the beam initialization: $\pm 45^\circ$ or $\pm 22^\circ$ of initial divergence and of 0° or 23° of inclination with the respect to target normal. Bremsstrahlung and K_α generation were simulated using the physics libraries Penelope and Livermore.[26] Simulations were conducted by launching 22 monochromatic beams with logarithmic-spaced energies from 5 up to 300 keV. The 2D Maxwellian $f_e(N_e, T_h, E) = \frac{N_e}{T_h} e^{-E/T_h}$ that reproduces both the bremsstrahlung spectrum $f_{ph}(E)$ on the BMXS and the K_α signal on the ZnVH is then reconstructed. In the function, N_e represents the total number of electrons and T_h the temperature.

Concerning the bremsstrahlung spectrometers, as shown in Sec. III A, three possible photon distribution functions are considered.

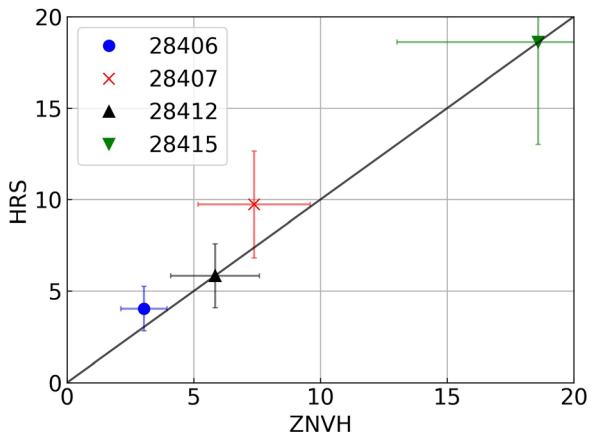

FIG. 8. Ratio between the signal detected by the HRS and ZnVH, normalized by 10^{10} ph/sr. The two spectrometers yield data consistent with each other.

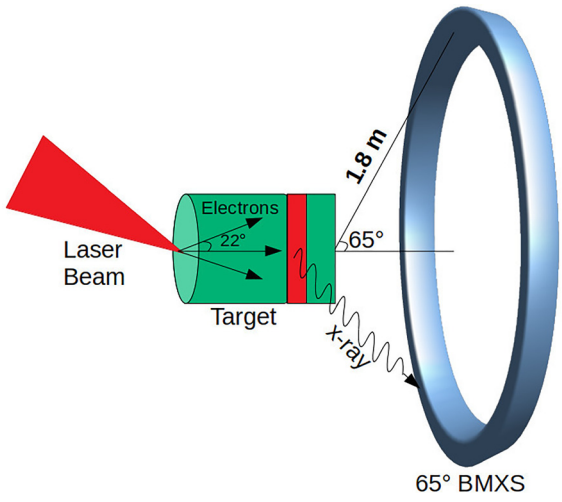

FIG. 9. Schematic illustration of target and detector configuration set in Geant4 simulation.

TABLE II. Coefficients N_e and T_h of the electron distribution functions $f_e(E)$ that generate the three $f_{ph}(E)$ detected by the 65° BMXS, for shot No. 28407, for all the possible combinations of initial beam divergences and incidences.

Electron spectra $f_e(E)$ Initial divergence	Beam incidence	N_{e1} (10^{16})	$f_{e1} \rightarrow f_{ph1}$ T_{h1} (keV)	N_{e2} (10^{16})	$f_{e2} \rightarrow f_{ph2}$ T_{h2} (keV)	N_{e3} (10^{16})	$f_{e3} \rightarrow f_{ph3}$ T_{h3} (keV)
22°	0°	4.0	22	1.3	31	0.5	43
45°	0°	4.2	22	1.3	32	0.6	42
22°	23°	4.2	22	1.3	32	0.5	43
45°	23°	4.0	22	1.3	32	0.5	43

Table II shows the electron distribution functions $f_e(N_e, T_h, E)$ that generate the three photon distributions $f_{ph}(E)$ on the 65° BMXS for shot No. 28407. Since no significant differences were observed between the two physics libraries in the simulation of the bremsstrahlung radiation, only the results from Penelope are shown. As can be observed, there are no remarkable differences between different initial divergences and inclinations of the input electron beam. The low mean kinetic energy of electrons leads to severe large-angle scattering that causes the particles to lose their directionality. This strengthens the initial assumption of cylindrical symmetry. As an example, Fig. 10 compares $f_{ph1}(E)$ and the simulated bremsstrahlung spectra produced on the 65° BMXS using the f_{e1}(E). For these particular target configurations and energy ranges, the photon distribution produced by an exponential distribution function of electrons has the form of $f_{ph}(E) = \frac{A_{ph}}{E} e^{-E/T_{ph}}$. This justifies the initial choice of fitting the BMXS signal with these kind of functions (see Sec. III A). Across all shots, it is possible to observe an average electron temperature T_h that spans from 20 up to 45 keV, with absolute number of electrons N_e ranging from 5×10^{15} up to 5×10^{16}.

Concerning the K_α simulations, similarly to the generation of the bremsstrahlung spectrum, the initial configurations of the electron beam is not seen to influence the K_α emission. Therefore, only results from the simulations with ±22° initial divergence and at normal incidence beam are reported. Figure 11 shows the possible values of N_e and T_h that reproduce the K_α signal on the ZnVH, combined with the values obtained previously by the BMXS, for the shot Nos. 28406 and

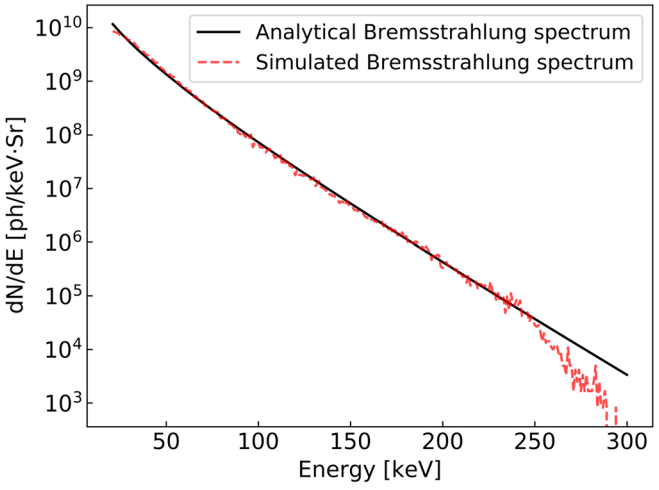

FIG. 10. Comparison of the bremsstrahlung spectra $f_{ph1}(E)$ in black and simulated one resulting from $f_{e1}(E)$ reported in Table II in red. The bremsstrahlung spectra comes from the post-processing of the 65° BMXS for the shot No. 28407. The laser to hot-electron energy conversion efficiency is ∼11% for the curve $f_{e1}(E)$.

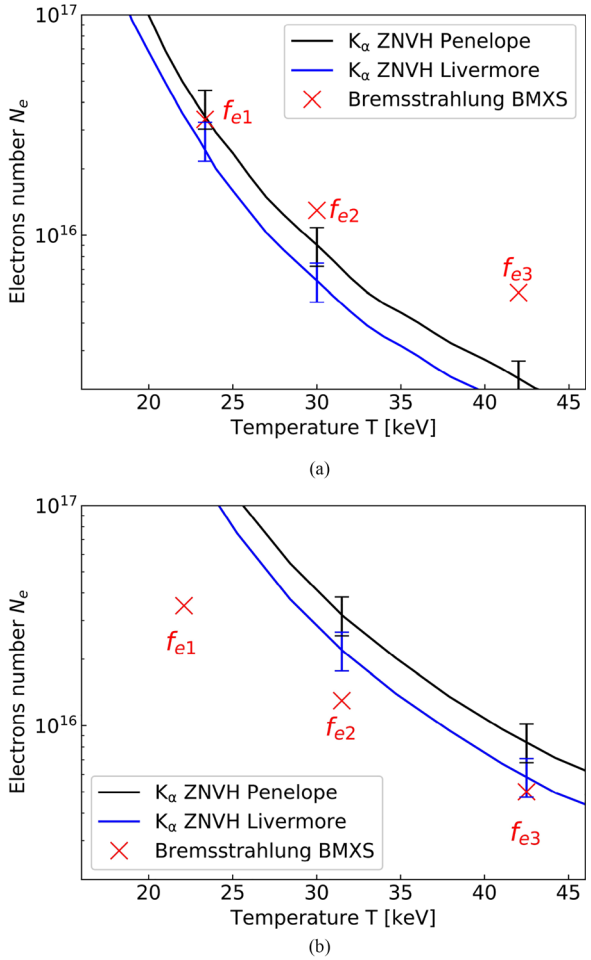

FIG. 11. Map of the possible values of N_e and T_h that can reproduce the experimental data (K_α and bremsstrahlung spectrum) for shot Nos. 28406 (a) and 28407 (b). The black and the blue lines result from K_α simulations with libraries Penelope and Livermore, respectively. The red crosses indicate the average values coming from the two BMXS, using the three representative points scheme. The experimental error on the K_α signal, evaluated to be around 20%, is shown by error bars.

28407. A disagreement of about 25% is found between the libraries Livermore and Penelope in reproducing the K_α. Since they predict that the same amount of electrons reaches the copper with identical energy distribution, the discrepancy must be attributed to differences in the computation of the cross section for the K-shell ionization $\sigma_k(E)$. These differences are, however, comparable to the relative standard deviation of the experimental measures of $\sigma_k(E)$.[27]

The disagreement between the results considering different shots does not allow to reduce the ranges of N_e and T_h. It is thus necessary to keep the three representative points considered in the analysis so far.

Figure 12 illustrates the conversion efficiency of laser energy into hot-electron energy for the five shots, considering for each the three possible f_e. Points in between are chosen in the case of significant discrepancies between the response of the BMXS and ZnVH (Fig. 11). In shots using a single interaction beam, three main regions can be identified: from 20 to 26 keV with efficiencies around 10%, from 27 to 35 keV with efficiencies around 6% and from 36 up to 45 keV with efficiencies around 2%–3%. The shots performed with two laser beams show similar conversion efficiencies and slightly higher temperatures.

In order to discriminate between the three regions, we use all these values as input of hydrodynamic simulations and we evaluate which reproduces the experimental evolution seen in the radiographs.

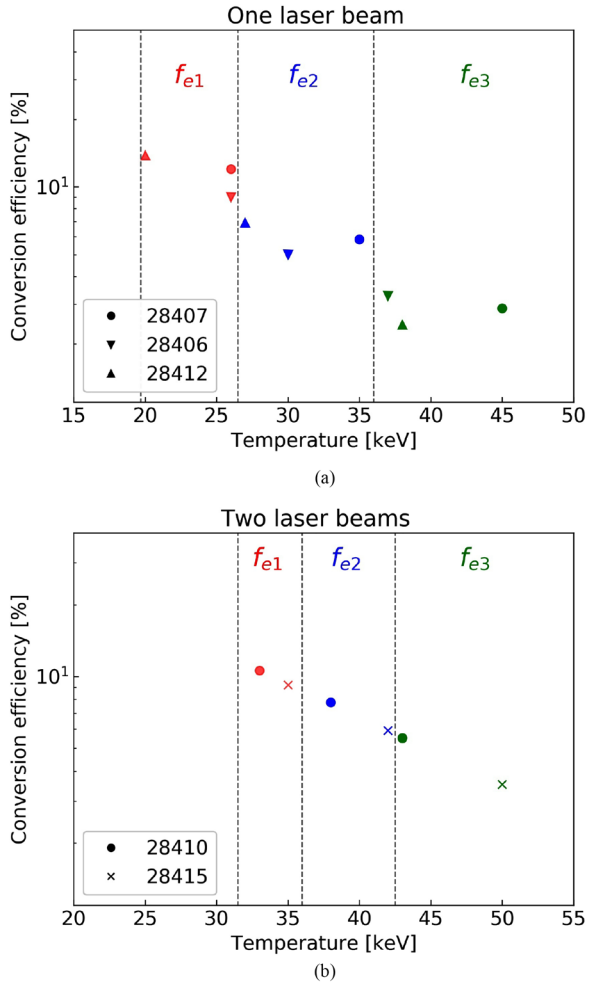

FIG. 12. Laser to hot-electron conversion efficiency as a function of temperature. Figure (a) reports the shots in which one beam was focused on target (1250 J): No. 28406, No. 28407, No. 28412. Figure (b) reports shot Nos. 28410 and 28415 with two laser beams (2500 J). The three main areas, corresponding to the three $f_e(E)$ detected by the BMXS and ZnVH, are reported in red, blue and green for each shot, respectively.

IV. HYDRODYNAMIC EVOLUTION OF TARGET AND EFFECT OF HOT ELECTRONS

A. Time-resolved radiographs

The shock propagation in the target was monitored by x-ray radiographs taken at different times. Figure 13 shows the array of sixteen radiographs captured by the XRFC for the shot No. 28407.

Among these, Fig. 14 shows the radiography at 250 ps and at 1.150 ns. At 250 ps, when the target is still cold, it is possible to see the CH ablator of 175 μm thickness, the copper plate of 20 μm, the plastic holder of 50 μm, and a $\sim$15 μm of glue between the holder and the copper. This indicates a correct alignment of the XRFC and a low value of parallax for the images of the third column of the array. In the radiograph at 1.150 ns, it is possible to discern the shock that propagates inside the ablator, although the poor contrast of the image makes the precise measurement of its position difficult. It is, however, clearly possible to see that the copper layer is thicker. Since at this time the shock did not reach the layer, such an expansion has been attributed to the effect of HE. The shock position and the copper plate expansion are the figures of merit considered to characterize the hot-electron

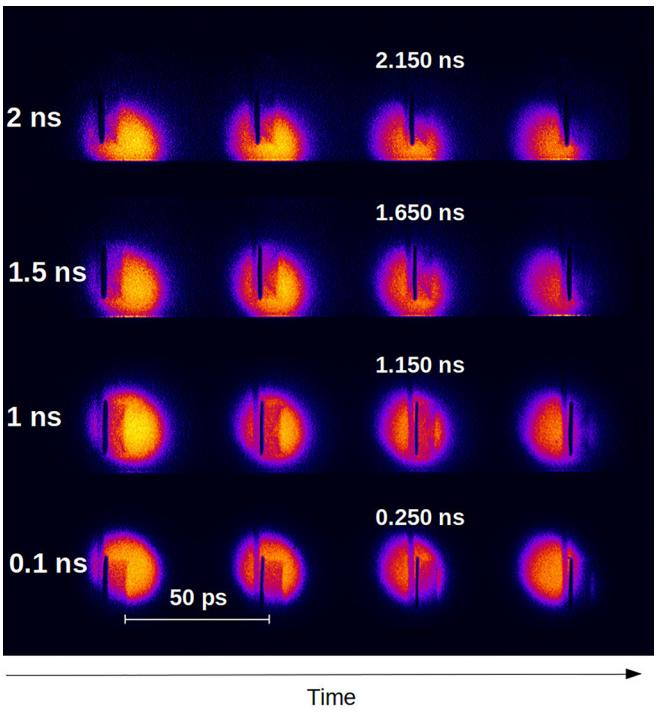

FIG. 13. Array of 2D radiographs captured at various times by the XRFC for shot No. 28407. Between each image on the line, there are 50 ps.

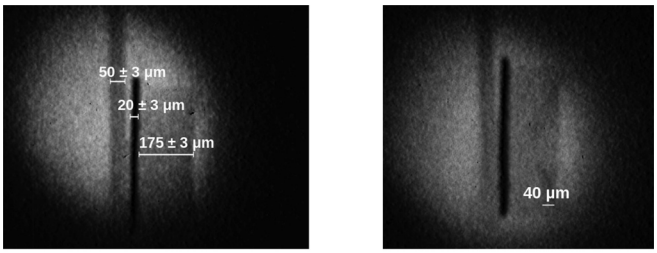

FIG. 14. Radiography of the target at 250 ps (a) and at 1.150 ns (b) for shot No. 28407. In the radiography (a), the thickness of the ablator, copper plate, and holder are indicated. Laser impinges on the right.

source. Different intensities and kinetic energies of the hot-electron beam will strongly affect the variation in time of these two quantities.

The expansion of the plate is evaluated by referring to transmissivity profiles taken along the cylinder axis, as shown in Fig. 15. The minimum in the curves indicates the presence of the copper and the FWHM represents its thickness. The transmissivity values were then normalized by the values resulting from the plastic holder. The holder remains un-compressed during the radiography, and we can hence assume that the x-ray flux that goes through it is constant and proportional to the backlighter emission.

B. Hydrodynamic simulations

Hydrodynamic simulations were performed with the 2D hydrodynamic code (CHIC)[28] developed at CELIA. The code describes single fluid two-temperatures hydrodynamics with thermal coupling between electrons and ions. Electron heat transport is described by the Spitzer–Harm model with flux limiter, while radiation transport is described by a multi-group approach using tabulated opacities. The calculation of hydrodynamic quantities relies on the equations of state taken from the SESAME database, and the ionization is calculated according to the Thomas–Fermi theory. The laser propagation is modeled using ray tracing accounting for inverse bremsstrahlung absorption. Losses due to stimulated Brillouin scattering (SBS) are not modeled. Since in our experiment the SBS reflected power was not directly measured, the experimental shape of the pulse was corrected by the amount of SBS evaluated by performing simulations with the

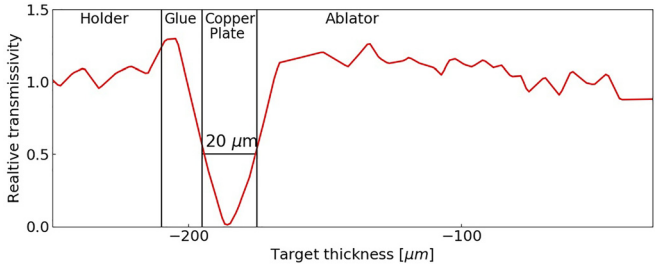

FIG. 15. Transmissivity profile on the cylinder axis extracted from the radiography at 250 ps for shot No. 28407. The position of ablator, copper plate, glue, and holder are indicated in the figure. The thickness of copper is measured by the FWHM of the transmissivity profile.

time-enveloped wave solver laser plasma simulation environment (LPSE).[29] This code couples the equations that describe the pump wave with the equations for the Raman and Brillouin scattered light and plasma waves. Plasma waves equations are solved around a given plasma frequency ω_{pe0}, whereas the Raman scattered field is enveloped at $\omega_r = \omega_0 - \omega_{pe0}$. The fluid equations for the plasma density and velocity govern the plasma dynamics. Coronal plasma density, velocity profiles, and electron temperatures at quarter critical density were extracted from an initial CHIC simulation with the experimental base pulse at four times: 0.3, 0.5, 0.9, and 1.3 ns. These parameters are then used as input for LPSE to calculate the percentage of SBS reflected light and study the Raman scattering at quarter critical density in one-dimensional geometry. The LPSE simulations run for 25 ps, which is long enough to observe the saturation of Raman and Brillouin instabilities. Discussion on the results of such simulations lies beyond the purpose of this work.

Here, we only retain the fraction of the Brillouin back-scattered light when the saturation of the instability is reached. The amount of the Brillouin reflected light obtained in the four simulations is the 2%, 7%, 46%, and 2% of the incoming pump wave, respectively. The correction is done by interpolating linearly in time these percentages and subtracting the values to the base pulse. The total fraction of scattered power in the simulation is around 20%. The shapes of experimental (red line) and the SBS-corrected (orange line) pulses are shown in Fig. 16(a).

Hot-electron propagation in the hydrodynamic simulation is modeled using the hot-electron transport package implemented in CHIC. Electrons propagate along straight lines depositing energy into the mesh according to the plasma stopping power formulas.[30,31] Straggling and blooming of the beam are taken into account by using the Lewis' model.[32] Further details are reported in Appendix. Electrons are described by a 2D Maxwellian function $f_e(N_e, T_h, E) = \frac{N_e}{T_h} e^{-E/T_h}$ in which the parameters N_e and T_h are taken from experimental data. The parameter N_e is related to laser-HE conversion efficiency η (see Sec. III C). This coefficient and the position where the HE source is initialized are modeled using the signal obtained by the SABS, as explained following. As shown by Fig. 17, this diagnostic detects light generated by absolute and convective SRS and the $\omega/2$ TPD signal. From Fig. 17, it is possible to see that the strongest signal is the broad spectral features characteristics of convective SRS, while the $\omega/2$ signal produced by TPD is weaker. The centers of the convective SRS emissions are around 625 and 575 nm for shot Nos. 28407 and 28410, respectively. According to the relation between the wavelength of backward scattered SRS and the density at which the scattering occurs[33]

$$\lambda_{SRS} = \lambda_L \left[1 - \sqrt{\frac{n_e}{n_c}\left(1 + 3k^2\lambda_D^2\right)}\right]^{-1}, \tag{3}$$

we can estimate that the average SRS emission happens at $0.14n_c$–$0.18n_c$. In the simulations, electron beamlets are thus initialized at $0.14n_c$ with an initial divergence of $\pm 22°$. This approach does not consider electrons generated at n_c by the Resonant Absorption (RAB) and at $n_c/4$ by the TPD. Nonetheless, different positions of the electron beam initialization do not influence the final results of the simulation. This is because electrons are initialized with a small angle of divergence and they will not lose a large amount of energy in the corona. The intensity of the electron beam is modeled in time considering the conversion efficiency $\eta(t)$ that follows temporally either the signal

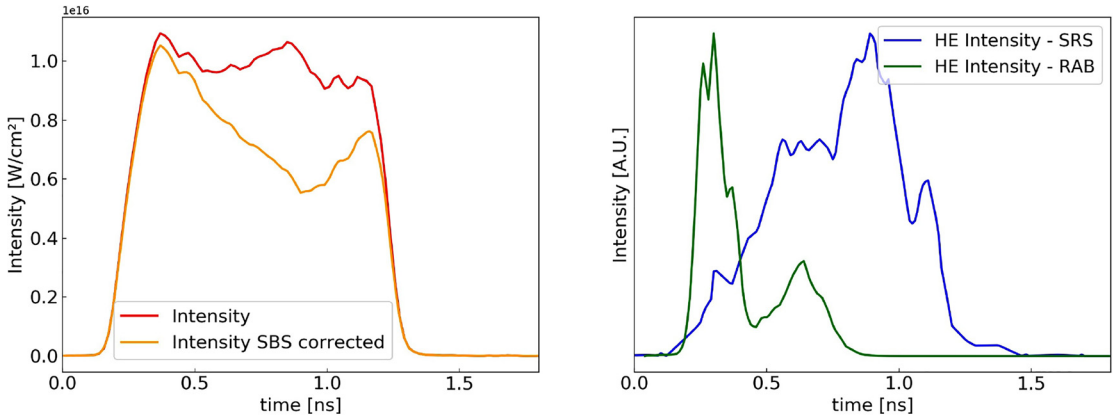

FIG. 16. (a) Experimental laser pulse shape (red) and SBS-corrected laser pulse shape (orange). (b) The intensity of HE beam is assumed to exactly follow either SRS reflected power measured by the SABS (blue) or RAB signal computed by CHIC (green).

measured by the SABS or the RAB signal computed by CHIC, as shown in Fig. 16(b). In particular, the signals were renormalized and rescaled considering the conversion efficiency given by BMXS and ZnVH (11%, 6%, 3% for the shot No. 28407, see Sec. III C). A discussion on the mechanisms of fast electron generation is currently an open topic, and it is out of the scope of the paper. Here, we limit our analysis to the characterization of hot electrons, focusing our attention on their effects on the hydrodynamic evolution of the target.

Three different CHIC simulations are performed in order to determine which combination of conversion efficiency η and average temperature T_h better reproduces the experimental behavior. The three corresponding $f_e(E)$ are reported in Table III.

C. Comparison between experimental and synthetic radiographs

The generation of synthetic radiographs from simulations is accomplished by reproducing the 3D cylindrical density profiles and then by calculating the theoretical transmissivity maps at the times of interest, according to the below formula:

$$T(t,x,y) = \exp\left[-\left(\frac{\mu}{\rho}\right)\int \rho(z)\mathrm{d}z\right]. \quad (4)$$

In the latter, $\rho(z)$ is the density of the material along the radiography axis and $\frac{\mu}{\rho}$ is the mass absorption coefficient in plastic and copper. The images are then blurred with a 2D Gaussian convolution with standard deviation of 15 μm to take in account the spatial resolution of the pinhole array. Transmissivity profiles are then extrapolated along the cylinder axis to evaluate the copper plate expansion. The values are renormalized by the transmissivity of the holder to be consistent with the experimental analysis.

To retrieve information on the hot-electron beam, we rely on the radiography taken at 1.650 ns, when the laser interaction is finished and hot electrons have already deposited their energy in the target.

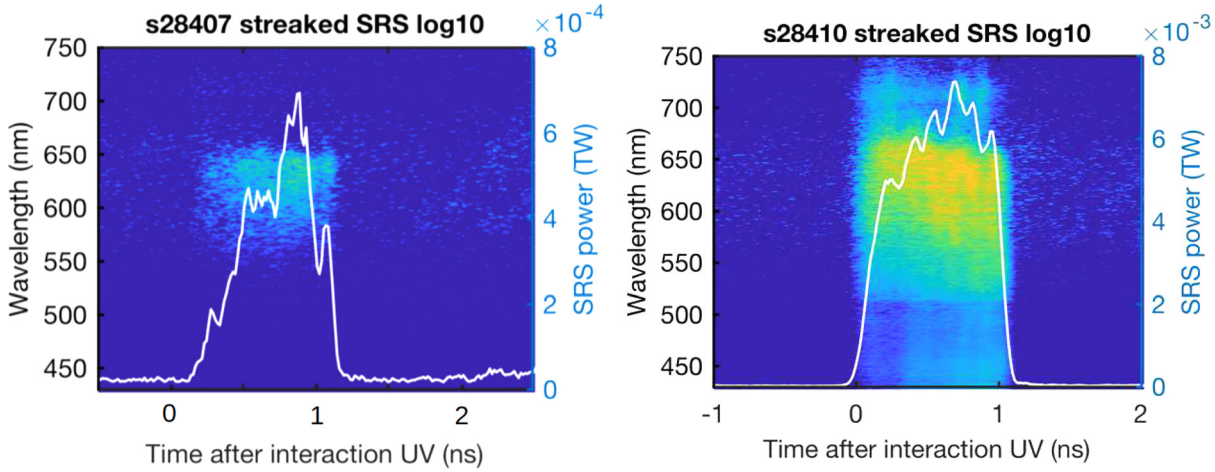

FIG. 17. Reflected light due to SRS and TPD collected by the SABS for shot Nos. 28407 and 28410. The bandwidth of the diagnostic ranges from 400 up to 750 nm. The temporal profile of the signal is indicated by the white line. The values of the SRS power collected are not significative, since the diagnostic covers only the 6% of the beam solid angle.

TABLE III. Parameters of Maxwellian functions $f_e(E)$ obtained from the post-process of BMXS and ZnVH for the shot No. 28407, used as input in CHIC.

f_e	T_h (keV)	η (%)	$N_e(10^{16})$
$f_{e1}(E)$	26	11	3.4
$f_{e2}(E)$	35	6	1.4
$f_{e3}(E)$	45	3	0.5

The experimental thickness, evaluated from the transmissivity curves, is $34 \pm 3\,\mu$m. Considering a diagnostic temporal resolution of ± 50 ps, Fig. 18 shows the superposition between the experimental curve at 1.650 ns and the numerical ones for a time windows that spans from 1.600 up to 1.700 ns. Three hot-electron cases (denoted with the corresponding f_{e_i}) and the case without hot electrons (woHE) are reported. The figures report the simulations with the hot-electron beam that follows temporally the SRS signal [blue curve in Fig. 16(b)]. We do not report the figures in which hot electrons follow the RAB signal [green curve in Fig. 16(b)], since the results are similar to the SRS case. This is likely due to the fact that we are considering the radiography at 1.650 ns, when the laser pulse is finished. At this time, the shock position and the copper thickness depend strongly on the intensity and on the mean kinetic energy of hot electrons (i.e., on the total preheat induced by HE); instead, the temporal shape of the beam (i.e., the hot-electron injection time) plays a second order effect.

The decrease in the synthetic transmissivity in the ablator is due to the presence of the shock that compresses matter. This effect allows to see the shock front propagating in the ablator in the cases f_{e_3} and woHE, while in the other two cases the shock has already reached the copper plate at 1.650 ns. In the experimental curves, this behavior is not observed and, on the contrary, the values coming from the compressed ablator are slightly higher compared to ones coming from the un-compressed holder. This is possibly due to nonuniformities in x-ray beam generated by the backlighter. While this issue makes the precise detection of the shock position difficult, it does not affect the information related to the copper thickness. From Fig. 18, it is possible to observe that the low temperature HE distributions (f_{e_1}, f_{e_2}) reproduce an expansion of the plate that approaches the experimental behavior. For the other cases (f_{e_3}, woHE), the expansion is lower and not compatible with experimental results. For the case woHE, the shock front approaches the copper plate at t = 1.900 ns. The copper expansion taken at this time for this particular case is $\sim 25\,\mu$m.

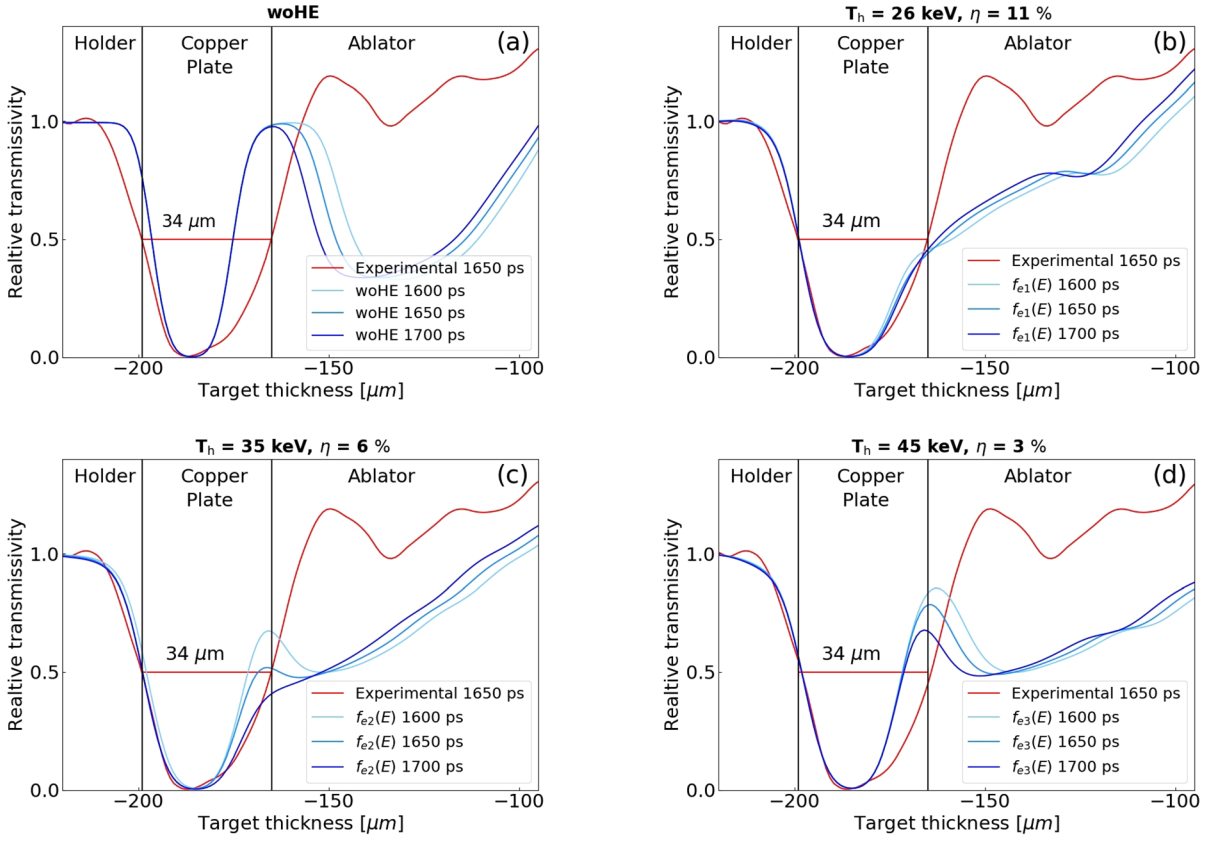

FIG. 18. Transmissivity curves taken along the central axis. In red the experimental curve extracted from the radiography at 1.650 ns for shot No. 28407, in blue the synthetic curves for time window that spans from 1.600 up to 1.700 ns. The four figures correspond to the four simulated cases: (a) case without HE; (b) simulation with hot-electron beam $f_{e1}(E)$; (c) simulation with hot-electron beam $f_{e2}(E)$; (d) simulation with hot-electron beam $f_{e3}(E)$. In these simulations, the hot-electron beam follows temporally the SRS signal [blue curve in Fig. 16(b)].

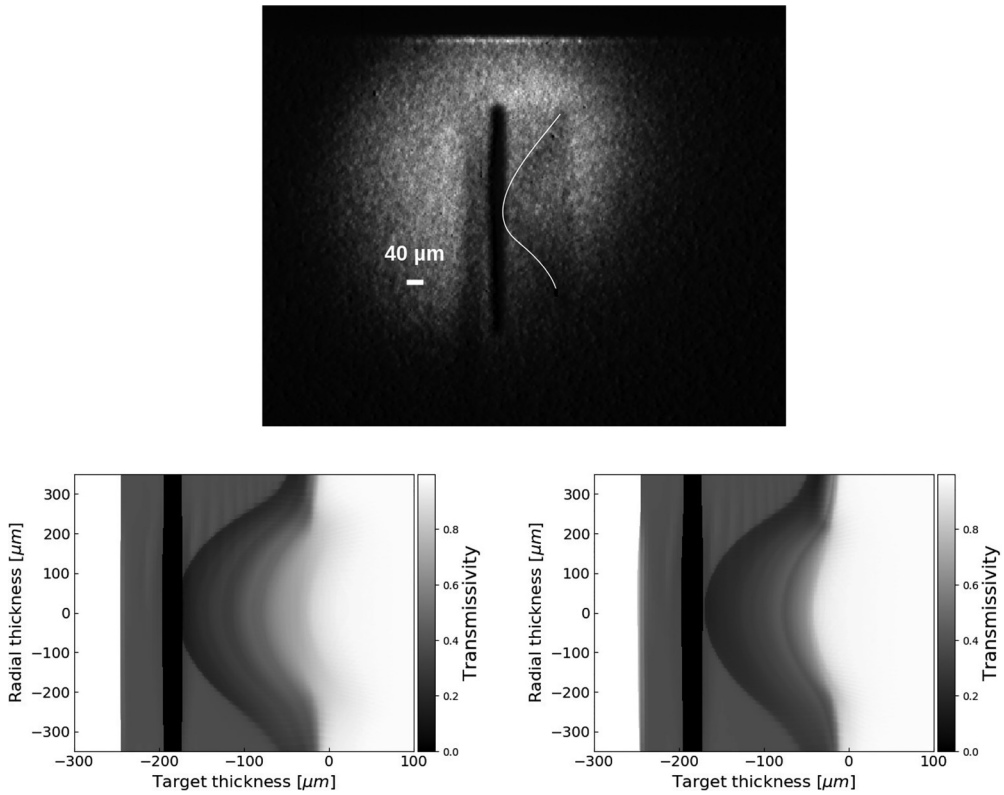

FIG. 19. (Top) Experimental radiography of shot No. 28407 at 1.650 ns. The shock front is highlighted; (bottom-left) synthetic radiography obtained by the simulation with $f_{e1}(E)$ at t = 1.700 ns; (bottom-right) synthetic radiography obtained by the simulation with $f_{e2}(E)$ at t = 1.700 ns.

This indicates that the copper expansion driven only by the radiative transport plays a minor role compared to the expansion due to the hot-electron energy deposition.

The experimental radiography at 1.650 ns is illustrated in Fig. 19. At that time, the shock front is into the copper plate. We report in the same figure the synthetic radiographs obtained from the simulations with $f_{e1}(E)$ and $f_{e2}(E)$ at 1.700 ns, considering as before the limit in the time resolution of the camera. In the case $f_{e2}(E)$, the shock is approaching the plate, while in the simulation with $f_{e1}(E)$ the shock is already propagating inside, in agreement with the experimental behavior. In the other two cases [without HE and $f_{e3}(E)$], the shock at 1.700 ns has not yet reached the plate. As such, the 2D x-ray radiography suggests that the HE distributions $f_{e1}(E)$ and $f_{e2}(E)$ are more consistent with the experimental results.

The conclusions presented from the time-gated radiography are strengthened by results from the 1D time-resolved radiography, shown in Fig. 20 for shot No. 28412. This figure shows the ablator of 175 μm, the ablation zone that grows in time and the copper plate. The progression of the shock into the target is indicated by the white-dashed line in Fig. 21, in which we compare the experimental radiography with the synthetic ones. Despite the large error bars due to low contrast of the experimental image, there is an indication that lower temperatures and higher efficiencies are more appropriate to reproduce the experimental behavior.

In conclusion, the simulation with the HE distribution $f_{e1}(E)$ is better in agreement with experimental results, either considering the 2D radiography and the 1D time-resolved radiography. The behavior predicted by the simulation with $f_{e2}(E)$ approaches the experimental results, while the simulations with $f_{e3}(E)$ and without HE beam are clearly not in agreement with experiment. Considering $f_{e1}(E)$ and $f_{e2}(E)$ as the closer to experimental results, we identify a hot-electron temperature $T_h = 27 \pm 8$ keV and a conversion efficiency $\eta = 10\% \pm 4\%$. These ranges correspond to the first two zones (f_{e1} and f_{e2}) of Fig. 12(a). For the shots in which two laser beams were used, the unavailability of exploitable radiographs does not allow to retrieve detailed information on the hot-electron beam.

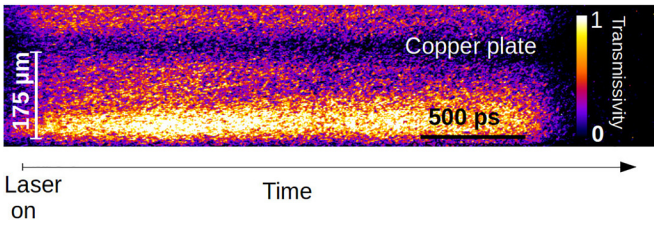

FIG. 20. Experimental time-resolved 1D radiography in the shot No. 28412. Time is on the x axis. Laser impinges from the bottom.

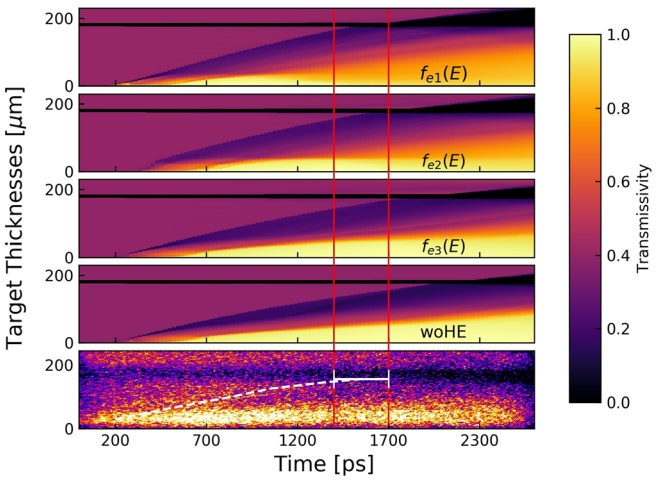

FIG. 21. Comparison between the experimental 1D time-resolved radiography of shot No. 28412 and the synthetic ones. The three hot-electron cases (denoted f_{e_i}) and the without HE (woHE) case are reported. The time at which the shock arrives on the plate is marked with red lines. The white dashed line indicates the progression of the shock.

D. Temperature of the copper plate

The K_α spectra measured by the HRS are used to estimate the electronic temperature reached by copper during the irradiation. The spectrum measured by the HRS for shot No. 28407 is shown in Fig. 22 (red line). In the figure, it is possible to see the two peaks related to the de-excitation of the copper K_α, namely, $K_\alpha 1$ and $K_\alpha 2$, resolved by the instrument. The emission lines, in the case of cold material, are at 8.0478 keV for $K_\alpha 1$ and at 8.0278 keV for $K_\alpha 2$. The heating and the consequent ionization of the material due to the presence of hot electrons induce a wavelength shift of the emission that results in broadening of the peaks.[34] Since the position of the HRS pointed to the front side of the target, the measured temperatures are referred to the first layers of the plate. This is because the K_α signal coming from those layers is stronger and less attenuated by the target itself. The experimental broadening is compared with synthetic signals simulated using the PrismSpect code.[35] These synthetic signals are reproduced considering the emission of K_α at different copper temperatures.

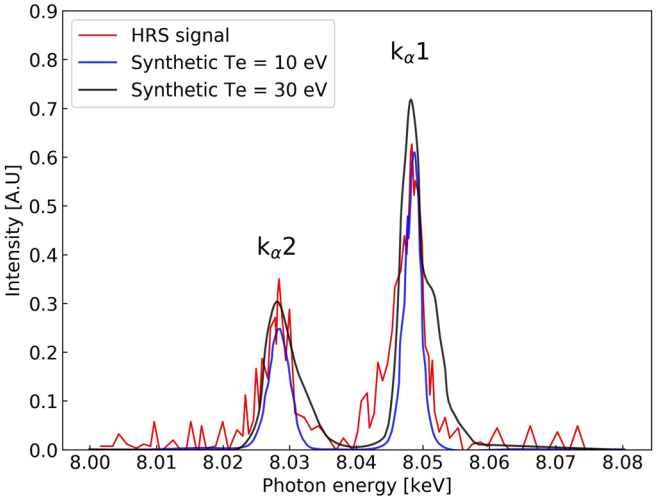

FIG. 22. Experimental and synthetic K_α spectra superimposed. The experimental signal in red refers to the shot No. 28407. The synthetic signal are reproduced considering electronic copper temperatures between 10 (blue curve) and 30 eV (black curve).

As shown in Fig. 22, the broadening of the peaks indicates temperatures greater than 10 eV, but lower than 30 eV. The copper temperature computed by CHIC for simulations with HE presents its maximum of 13 eV in the first part of the plate, decreasing down to 5 eV in the rear side. The values provided by the simulation without HE are 0.2 eV. The values predicted by the simulations with hot electrons are thus in much better agreement with the experimental results.

V. INFLUENCE OF HOT ELECTRONS ON THE HYDRODYNAMIC AND DISCUSSION

We now analyze the simulation results that matches the experimental data. As explained in Sec. IV, the laser pulse used as input in the simulations follows temporally the experimental pulse, after a correction taking into account the SBS reflection. The SBS fraction was calculated performing LPSE simulations considering hydrodynamic profiles extracted by an initial CHIC simulation at different times (see Sec. IV B). The SBS removed power corresponds to ∼20% of the total power. Hot electrons are generated at $0.14n_c$ following the temporal profile of the backscattered light measured by the SABS instrument. HE beams are energetically described by exponential distributions characterized by $T_h = 26$ keV and conversion efficiency with respect to the laser energy of $\eta \simeq 11\%$. We consider that an equal fraction of scattered light through SRS occurs, so an additional 11% of light at $n_c/4$ is backscattered and subtracted from the laser. The RAB fraction computed by the code is only the 0.33%, while the collisional absorption is around ∼58%.

In the simulation, electrons propagate according to straight lines, with an initial divergence of the beam of 22° (see Appendix).

The simulations without hot electrons is also presented, and for this case, the fraction of collisional absorption computed by the code is ∼95% (after the subtraction of the SBS part).

1. Plasma parameters

The $n_c/4$ density-scale length rises up to 150 μm in the first 0.8 ns, while the $n_c/4$ coronal electronic temperature reaches ∼2.1 keV in the first 0.6 ns, as shown in Fig. 23. Considering the temporal evolution of these parameters, the intensity threshold for SRS[36] and TPD[37] are exceeded after ∼200 ps, i.e., almost at the begin of the drive laser pulse.

2. Shock characteristics

Figure 24 shows the temporal progression of different hydrodynamic quantities around the shock front. The results from simulations with and without hot electrons are presented. The ablation pressure reaches a maximum of 100 mbar at 0.3 ns for the two cases, regardless of the presence of the hot-electron beam. These values are four times less compared to the value of ∼400 mbar predicted by the scaling laws $p_{abl} \propto \lambda^{-2/3} I_a^{2/3}$, observed for laser intensities of 10^{15} W/cm^2.[38] This mismatch is due to the fact that the

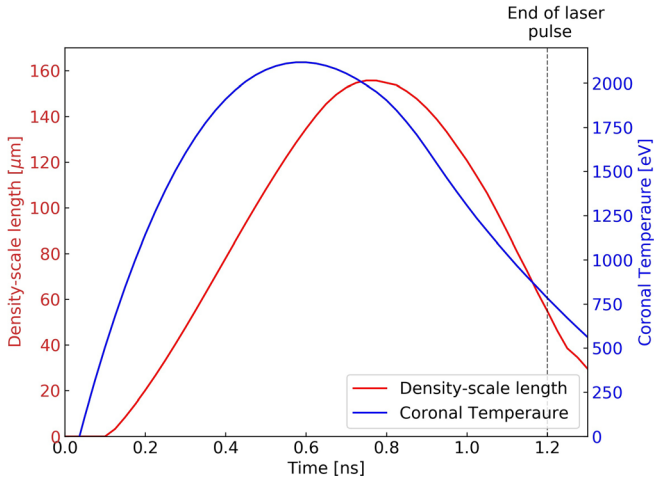

FIG. 23. Evolution in time of the density-scale length and coronal electronic temperature computed at $n_c/4$. The time interval considered corresponds to the time of SRS activity observed in the SABS.

scaling law considers 1D collisional laser absorption without parametric instabilities and nonthermal electrons. Despite this, the obtained values of ablation pressure are in agreement with other planar configurations experiments.[3,39]

Considering that 175 μm of cold plastic stops electrons up to 100 keV, it is possible to estimate that 98% of electrons in the experiment are stopped in the ablator. This increases the electronic temperature and pressure reached by the ablator upstream of the shock, 9 eV and 11 mbar, respectively. The value of temperature is evaluated 50 μm upstream of the shock and the value of pressure is calculated considering the minimum around the shock front. The position of the shock front is computed considering the maximum of the derivative of the logarithm of the pressure. The downstream pressure reaches a maximum of 150 mbar, 25 mbar more than without HEs. The downstream pressure is calculated considering the maximum pressure after the shock front. The increase in the downstream pressure, driven by the presence of electrons, is beneficial for the SI scheme. The shock strength, which is the ratio between the downstream and the upstream pressures at the shock front, decreases dramatically from ∼700 for the case without HE to ∼20 for the simulations with HE. The shock velocity in the presence of HEs increases from 100 to 130 km/s.

3. Comparison with other SI experiments

Compared with a recent shock ignition experiment carried out in OMEGA,[40] our analysis shows similar hot-electron temperature, but conversion efficiency ten times higher. In that experiment, an UV ($\lambda = 0.351$ μm) interaction beam was focused on the CH ablator of a multilayer planar target after plasma-creation beams of lower intensity.

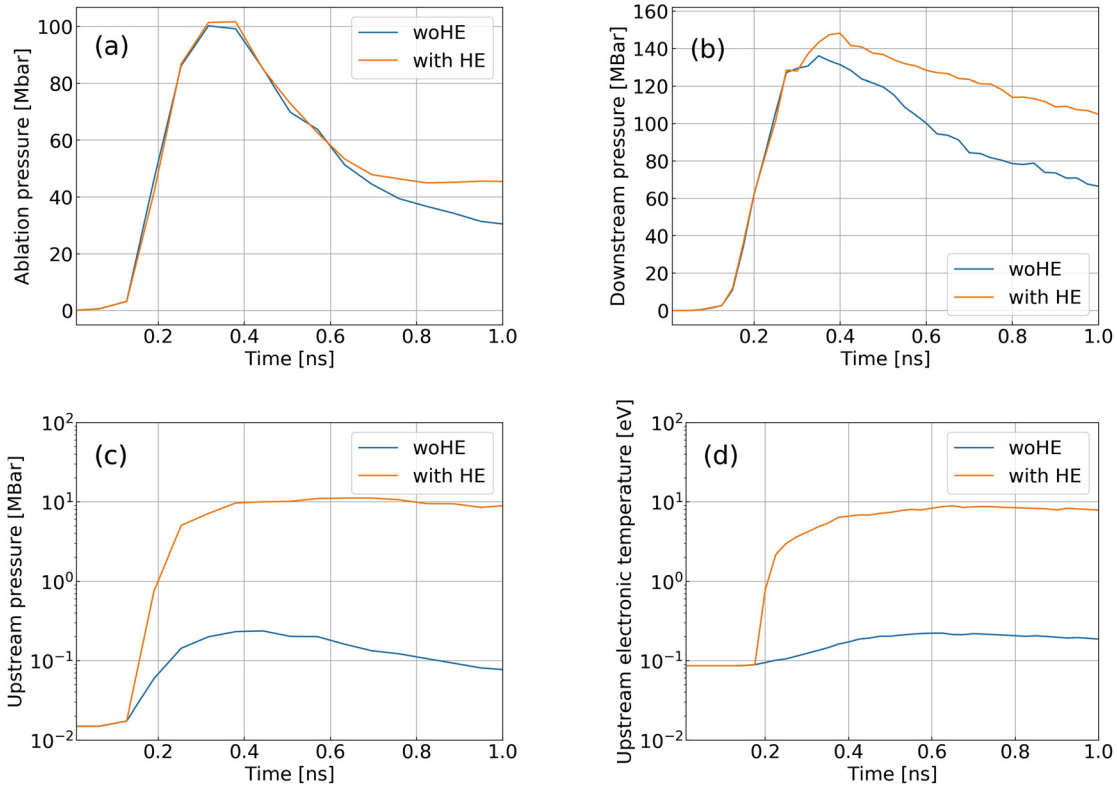

FIG. 24. Evolution in time of hydrodynamic quantities around the shock position resulting from CHIC simulations. The simulation with HE (orange) and without HE (blue) are reported. (a) Ablation pressure; (b) downstream pressure; (c) upstream pressure; and (d) upstream electronic temperature. Hot electrons are described by a Maxwellian function with $T_h = 26$ keV and laser to hot-electron conversion efficiency $\eta \sim 11\%$.

The parameters of the interaction beam were similar to our case: 1-ns square pulse 23° off the target normal, for a vacuum intensity of $\sim 10^{16}$ W/cm^2. The plasma was characterized by a scale length of $\sim 330\ \mu$m and a coronal electronic temperature of 1.8 keV. The difference in the conversion efficiencies between the two experiments could be due to the influence of longer plasma scale-lengths on the LPIs. Low HE temperatures of ∼30 keV are also reported in spherical configuration experiments.[41] In this case, 40 of the 60 OMEGA beams were used to compress D_2 filled plastic shells. The remaining 20 spike beams were delayed and tightly focused onto shell to deliver a late shock. The intensity of the single spike beam was several 10^{15} W/cm^2, interacting with a plasma characterized by $L_n \sim 170\ \mu$m and T_e ∼2 keV. As such, we can observe that, in this particular regime, the HE temperature does not depend on laser intensity, in agreement with recent theoretical expectations (see, for instance, Ref. 42). On the contrary, higher temperatures were found in experiments in which different laser beams were overlapped during the interaction.[39,43] These experiments were characterized by longer scale-lengths (L_n ∼350–400 μm) but lower laser intensities (∼10^{15} W/cm^2, 1–7 × 10^{14} W/cm^2, respectively).

References 14 and 44 report the results of a recent experiment conducted at the NIF.[45] In this experiment, planar targets were irradiated using the 64 "outers" or the 32 "inner" beams configurations for an overlapped intensity ranging from ∼4 × 10^{14} up to 15 × 10^{14} W/cm^2. The $n_c/4$ density scale length and coronal temperature reached in these conditions were ∼500–700 μm and 3–5 keV. Hot-electron temperatures of ∼40 to 60 keV with conversion efficiencies of ∼0.5% up to 5% were obtained when the intensity increased from 4 up to 15 × 10^{14} W/cm^2. Authors suggest that SRS is the dominant mechanism in the generation of fast electrons. The differences in conversion efficiencies and electron energy compared to our experiment is due to the different processes that rule the hot-electron generation in the presence of longer scale length and higher coronal temperatures. These aspects are an open problem under investigation.[46]

4. Effects of hot electrons on the implosion scheme

In Ref. 6, a theoretical study on the implosion of a spherical target is presented. The target is composed of an high Z ablator of 15 nm (Al 2.7 g/cc), a plastic ablator of 31 μm (CH 1.05 g/cc), a dense ice shell of 220 μm (DT-ice 0.254 g/cc) filled with 737 μm of gas (DT 10^{-4} g/cc). The sphere is irradiated by a compression beam followed by an ignitor spike (∼200 kJ launched after 13.6 ns). The results from CHIC simulations of the implosion are presented, considering or not the presence of hot electrons. The Maxwellian distribution function considered in the simulations with hot electrons is characterized by average temperatures of 43 and 98 keV, with conversion efficiencies of 1.2% and 0.94% of the total laser energy. In this configuration, after the compression phase, the areal density of the plastic ablator reaches values of ∼5 mg/cm^2 and it stops electrons up to 50–70 keV. Electrons up to 170 keV are stopped at beginning of the spike plateau in the dense shell, that reaches areal densities of 40–100 mg/cm^2. The shell adiabat calculated 200 ps after the spike rises from ∼1 in the case without hot electrons, up to ∼1.5 in the simulation with HE. This effect is related to the increase in the shell pressure due to the deposit of energy by the electron beam.

Let us now consider the same hydrodynamic setup, but applied to our results for the HE distribution. Considering the values of temperature obtained in our experiment (i.e., 26 keV), it is possible to estimate that 93% of electrons are stopped in the ablator, while 7% deposit energy in the shell. A shell adiabat of ∼2.4 is estimated 200 ps after the spike, rescaling the electron flux considering the laser energy proposed in the cited paper (i.e., 11% of 200 kJ). There we have used an ideal gas model to calculate the pressure reached by the shell due the deposit of energy by the electron beam. Despite the simplified model, the increase in the adibat warns that the high conversion efficiency found in the experiment could represent an issue for the SI scheme. More detailed investigations are required in this direction, taking into account the amplification of the shock pressure due to the presence of hot electrons that could balance the negative effects.

VI. SUMMARY AND CONCLUSIONS

Planar multilayer targets (CH 175 μm–Cu 20 μm) were irradiated with UV ($\lambda = 351$ nm) laser pulses at SI-relevant intensities (∼10^{16} W/cm^2). The plasma scale length and the coronal temperature computed at $n_c/4$ raised up to 150 μm and 2.1 keV, respectively. One additional laser beam was focused on V foil to produce He_α x rays to perform 2D time-gated and 1D time-resolved radiographs. The hot-electron population generated in the interaction is characterized in terms of intensity and temperature using different spectrometers. Two time-integrating hard x-ray spectrometers (BMXSs) were used to detect the bremsstrahlung radiation. Zinc von Hamos (ZnVH) and high-resolving-power (HRS) x-ray spectrometers were used to collet K_α signal coming from the transit of electrons in the copper tracer.

The interpretation and the post-processing of spectrometer data (BMXS and ZnVH) are based on MC methods, in which the 3D geometry of the target is reproduced and the response of the spectrometers is simulated. This procedure can be considered appropriate for a first-order interpretation of the results, even if the MC code does not account for the hydrodynamic evolution of the irradiated target. The interval of temperature indicated by the spectrometers ranges from 20 up to 50 keV, with an energy conversion efficiency that goes from 13% down to 2%. These data are used as input of hydrodynamic simulations reproducing the propagation of the shock in the target and the expansion of the Cu layer observed in the radiographs. In this regard, hydrodynamic simulations suggest that lower values of temperatures ($T_h = 27 \pm 8$ keV) and higher conversion efficiencies ($\eta = 10\% \pm 4\%$) are more appropriate. We thus emphasize the importance of the coupling between different diagnostics and numerical tools to sufficiently constrain the problem, not discarding *a priori* possible degenerate solutions coming from the chi-square analysis.

The simulation with HE beam with these parameters predicts a copper heating at the end of laser pulse in agreement with the temperature which can be inferred from the broadening of the K_α line as measured by the HRS spectrometer.

In our experiment, HE are found to increase the downstream pressure from about 125 to 150 mbar and the shock velocity from 100 to 130 km/s. Conversely, the deposition of energy upstream of the shock increases the pressure of the ablator, resulting in a dramatic decrease in the shock strength.

Simple estimation of the effect of the measured HE distribution into a typical SI design suggests a detrimental effect, but further investigations are required to understand the effects of the electron beam on the implosion scheme.

ACKNOWLEDGMENTS

This material is based on the work supported by the Department of Energy National Nuclear Security Administration under Award No. DE-NA0003856, the University of Rochester, and the New York State Energy Research and Development Authority. This report was prepared as an account of work sponsored by an agency of the U.S. Government. Neither the U.S. Government nor any agency thereof, nor any of their employees, makes any warranty, express or implied, or assumes any legal liability or responsibility for the accuracy, completeness, or usefulness of any information, apparatus, product, or process disclosed, or represents that its use would not infringe privately owned rights. Reference herein to any specific commercial product, process, or service by trade name, trademark, manufacturer, or otherwise does not necessarily constitute or imply its endorsement, recommendation, or favoring by the U.S. Government or any agency thereof. The views and opinions of authors expressed herein do not necessarily state or reflect those of the U.S. Government or any agency thereof.

This work has been carried out within the framework of the EUROfusion Enabling Research Project No. AWP17-ENR-IFE-CEA-01 "Preparation and Realization of European Shock Ignition Experiments" and has received founding from the Euratom research and training program 2014–2018 under Grant Agreement No. 633053. The views and opinions expressed herein do not necessarily reflect those of the European Commission.

AUTHOR DECLARATIONS

Conflict of Interest

The authors have no conflicts to disclose.

APPENDIX: MODELIZATION OF HOT-ELECTRON TRANSPORT IN CHIC

Hot electrons propagate along straight lines, depositing energy in the mesh according to the plasma stopping power formulas. Some angular scattering is, however, accounted for by widening the electron beam according the first transport scattering cross section (see at the end of this appendix). This approach has been validated against the M1 code.[47]

The stopping power formulas consider the loss of energy of the primary particle due to collisions with plasma free electrons, partially ionized atoms and excitation of plasma waves. The loss of energy due to electron–electron collisions reads[30]

$$\frac{\mathrm{d}E}{\mathrm{d}S_{ee}} = \frac{2\pi r_0^2 mc^2 n_e}{\beta^2}\left[\ln\left(\frac{(m^2c^2(\gamma-1)\lambda_D^2}{2\hbar^2}\right)+1 + \frac{1}{8}\left(\frac{\gamma-1}{\gamma}\right)^2 - \left(\frac{2\gamma-1}{\gamma^2}\right)\ln 2\right]. \tag{A1}$$

The loss of energy due to collision between the electron and partially ionized atoms is calculated according the Bethe formula, in which the mean excitation potential I is modeled to account for the degree of ionization of ions,

$$\frac{\mathrm{d}E}{\mathrm{d}S_{ei}} = \frac{2\pi r_0^2 mc^2 (Z-Z^*)n_i}{\beta^2}\left\{\ln\left[\left(\frac{E_k}{I}\right)^2\frac{(\gamma+1)}{2}\right] + \frac{1}{\gamma^2} + \frac{1}{8}\left(\frac{\gamma-1}{\gamma}\right)^2 - \left(\frac{2\gamma-1}{\gamma^2}\right)\ln(2)\right\}. \tag{A2}$$

The formula used to model I is

$$I = aZ\frac{\exp\left[1.294\left(\frac{Z^*}{Z}\right)^{0.72-0.18(Z^*/Z)}\right]}{\sqrt{1-\frac{Z^*}{Z}}}, \tag{A3}$$

in which $a \sim 10$ eV, Z is the atomic number of the considered species, and Z^* is the ionization state.[48] This formula comes from the fitting of theoretical calculations of $I(Z, Z^*)$ based on the Thomas–Fermi theory.

Fast electrons excites plasma oscillations in the neighborhood of their path. The loss of energy related to this effect is described by[49]

$$\frac{\mathrm{d}E}{\mathrm{d}S_{ep}} = \frac{2\pi r_0^2 mc^2 n_e}{\beta^2}\ln\left(1.123\frac{\beta c}{\omega_p \lambda_D}\right)^2. \tag{A4}$$

The total stopping power is derived by adding the three contributions,

$$S_e(E) = \frac{\mathrm{d}E}{\mathrm{d}S_{ee}} + \frac{\mathrm{d}E}{\mathrm{d}S_{ei}} + \frac{\mathrm{d}E}{\mathrm{d}S_{ep}}. \tag{A5}$$

The diffusion is modeled considering the mean diffusion angle obtained by the Lewis' theory,[32]

$$\langle\cos\theta\rangle(s) = \exp\left[-\int_0^s k_1(s)\mathrm{d}s\right], \tag{A6}$$

where $k_1(s)$ is the inverse of the first transport path. Assuming that the particles in the beam propagate along straight line in the z direction, the energy loss rate reads

$$\frac{\mathrm{d}E}{\mathrm{d}z} = -\frac{1}{\langle\cos\theta\rangle(s)}S_e(E). \tag{A7}$$

An additional energy loss is accounted in the transverse direction of thickness Δ,

$$\frac{\mathrm{d}\Delta}{\mathrm{d}z} = 2\langle\tan\theta\rangle(s). \tag{A8}$$

DATA AVAILABILITY

The data that support the findings of this study are available from the corresponding author upon reasonable request.

REFERENCES

[1]V. A. Shcherbakov, "Ignition of a laser-fusion target by a focusing shock wave," Sov. J. Plasma Phys. **9**(2), 240–241 (1983).
[2]R. Betti, C. D. Zhou, K. S. Anderson, L. J. Perkins, W. Theobald, and A. A. Solodov, Phys. Rev. Lett. **98**, 155001 (2007).
[3]D. Batani, S. Baton, A. Casner, S. Depierreux, M. Hohenberger, O. Klimo, M. Koenig, C. Labaune, X. Ribeyre, C. Rousseaux *et al.*, Nucl. Fusion **54**, 054009 (2014).

[4]D. W. Forslund, J. M. Kindel, and E. L. Lindman, Phys. Fluids **18**, 1002 (1975).
[5]W. Kruer, *The Physics of Laser Plasma Interactions*, Frontiers in Physics Series (Westview Press, 2003).
[6]A. Colatis, X. Ribeyre, E. L. Bel, G. Duchateau, P. Nicolai, and V. Tikhonchuk, Phys. Plasmas **23**, 072703 (2016).
[7]S. Yu. Gus'kov, P. Kuchugov, R. Yakhin, and N. Zmitrenko, "The role of fast electron energy transfer in the problem of shock ignition of laser thermonuclear target," High Energy Density Phys. **36**, 100835 (2020).
[8]S. Yu. Gus'kov, X. Ribeyre, M. Touati, J.-L. Feugeas, P. Nicolai, and V. Tikhonchuk, Phys. Rev. Lett. **109**, 255004 (2012).
[9]S. Yu. Gus'kov, A. Kasperczuk, T. Pisarczyk, S. Borodziuk, M. Kalal, J. Limpouch, J. Ullschmied, E. Krousky, K. Masek, M. Pfeifer *et al.*, "Efficiency of ablative loading of material upon the fast-electron transfer of absorbed laser energy," Quantum Electron. **36**(5), 429–434 (2006).
[10]S. Y. Gus'kov, N. N. Demchenko, A. Kasperczuk, T. Pisarczyk, Z. Kalinowska, T. Chodukowski, O. Renner, M. Smid, E. Krousky, M. Pfeifer *et al.*, "Laser-driven ablation through fast electrons in PALS-experiment at the laser radiation intensity of 1–50 PW/cm^2," Laser Part. Beams **32**(1), 177–195 (2014).
[11]W. Theobald, R. Nora, W. Seka, M. Lafon, K. S. Anderson, M. Hohenberger, F. J. Marshall, D. T. Michel, A. A. Solodov, C. Stoeckl *et al.*, "Spherical strong-shock generation for shock-ignition inertial fusion," Phys. Plasmas **22**, 056310 (2015).
[12]L. Antonelli, J. Trela, F. Barbato, G. Boutoux, P. Nicolai, D. Batani, V. Tikhonchuk, D. Mancelli, A. Tentori, S. Atzeni *et al.*, Phys. Plasmas **26**, 112708 (2019).
[13]D. Batani, L. Antonelli, F. Barbato, G. Boutoux, A. Colaïtis, J.-L. Feugeas, G. Folpini, D. Mancelli, P. Nicolai, J. Santos *et al.*, Nucl. Fusion **59**, 032012 (2018).
[14]M. J. Rosenberg, A. A. Solodov, J. F. Myatt, W. Seka, P. Michel, M. Hohenberger, R. W. Short, R. Epstein, S. P. Regan, E. M. Campbell *et al.*, "Origins and scaling of hot-electron preheat in ignition-scale direct-drive inertial confinement fusion experiments," Phys. Rev. Lett. **120**(5), 055001 (2018).
[15]L. J. Waxer, D. N. Maywar, J. H. Kelly, T. J. Kessler, B. E. Kruschwitz, S. J. Loucks, R. L. McCrory, D. D. Meyerhofer, S. F. B. Morse, C. Stoeckl *et al.*, Opt. Photonics News **16**, 30 (2005).
[16]L. C. Jarrott, M. S. Wei, C. McGuffey, F. N. Beg, P. M. Nilson, C. Sorce, C. Stoeckl, W. Theoboald, H. Sawada, R. B. Stephens *et al.*, Rev. Sci. Instrum. **88**, 043110 (2017).
[17]P. M. Nilson, F. Ehrne, C. Mileham, D. Mastrosimone, R. K. Jungquist, C. Taylor, C. R. Stillman, S. T. Ivancic, R. Boni, J. Hassett *et al.*, Rev. Sci. Instrum. **87**, 11D504 (2016).
[18]C. D. Chen, J. A. King, M. H. Key, K. U. Akli, F. N. Beg, H. Chen, R. R. Freeman, A. Link, A. J. Mackinnon, A. G. MacPhee *et al.*, Rev. Sci. Instrum. **79**, 10E305 (2008).
[19]A. Curcio, P. Andreoli, M. Cipriani, G. Claps, F. Consoli, G. Cristofari, R. De Angelis, D. Giulietti, and F. Ingenito, J. Instrum. **11**, C05011 (2016).
[20]D. K. Bradley, P. M. Bell, J. D. Kilkenny, R. Hanks, O. Landen, P. A. Jaanimagi, P. W. McKenty, and C. P. Verdon, Rev. Sci. Instrum. **63**, 4813 (1992).
[21]O. V. Gotchev, P. A. Jaanimagi, J. P. Knauer, F. J. Marshall, and D. D. Meyerhofer, Rev. Sci. Instrum. **75**, 4063 (2004).
[22]G. Boutoux, D. Batani, F. Burgy, J. Ducret, P. Forestier-Colleoni, S. Hulin, N. Rabhi, A. Duval, L. Lecherbourg *et al.*, Rev. Sci. Instrum. **87**, 043108 (2016).
[23]S. Agostinelli, J. Allison, K. Amako, J. Apostolakis, H. Araujo, P. Arce, M. Asai, D. Axen, S. Banerjee, G. Barrand *et al.*, "GEANT4: A simulation toolkit," Nucl. Instrum. Methods Phys. Res., Sect. A **506**, 250 (2003).
[24]F. Salvat, *PENELOPE: A Code System for Monte Carlo Simulation of Electron and Photon Transport* (Nuclear Energy Agency, 2019).
[25]S. Pucella, *Fisica Dei Plasmi* (Zanichelli, 2014).
[26]S. T. Perkins, D. E. Cullen, M. H. Chen, J. Rathkopf, J. Scofield, and J. H. Hubbell, *Tables and Graphs of Atomic Subshell and Relaxation Data Derived from the LLNL Evaluated Atomic Data Library (EADL), Z = 1–100* (US Department of Energy, Office of Scientific and Technical Information, 1991).
[27]X. Llovet, C. Powell, F. Salvat, and A. Jablonski, J. Phys. Chem. Ref. Data **43**, 013102 (2014).
[28]J. Breil, S. Galera, and P.-H. Maire, Comput. Fluids **46**, 161–167 (2011).
[29]J. F. Myatt, J. G. Shaw, R. K. Follett, D. H. Edgell, D. H. Froula, J. P. Palastro, and V. N. Goncharov, J. Comput. Phys. **399**, 108916 (2019).
[30]A. Solodov and R. Betti, Phys. Plasmas **15**, 042707 (2008).
[31]R. M. More, "Plasma processes in non-ideal plasmas," in 29th Scottish Universities Sumner School in Physics Laser Plasma Interactions (1985).
[32]C. Li and R. Petrasso, Phys. Rev. E **73**, 016402 (2006).
[33]D. Watteau, in *La Fusion Thermonuclaire Inertielle Par Laser: Linteraction Laser-Matire Part 1*, French Edition, edited by CEA (CEA, 1991), Vol. 1.
[34]P. Palmeri, G. Boutoux, D. Batani, and P. Quinet, Phys. Rev. E **92**, 033108 (2015).
[35]J. J. MacFarlane, I. E. Golovkin, P. Wang, P. R. Woodruff, and N. A. Pereyra, High Energy Density Phys. **3**, 181 (2007).
[36]B. Afeyan and E. A. Williams, Phys. Fluids **28**, 3397 (1985).
[37]A. Colatis, G. Duchateau, X. Ribeyre, Y. Maheut, G. Boutoux, L. Antonelli, P. Nicolai, D. Batani, and V. Tikhonchuk, Phys. Rev. E **92**, 041101 (2015).
[38]J. Lindl, Phys. Plasmas **2**, 3933 (1995).
[39]M. Hohenberger, W. Theobald, S. X. Hu, K. S. Anderson, R. Betti, T. R. Boehly, A. Casner, D. E. Fratanduono, M. Lafon, D. D. Meyerhofer *et al.*, Phys. Plasmas **21**, 022702 (2014).
[40]S. Zhang, C. Krauland, J. Peebles, J. Li, F. Beg, N. Alexander, W. Theobald, R. Betti, D. Haberberger, M. Campbell *et al.*, Phys. Plasmas **27**, 023111 (2020).
[41]W. Theobald, R. Nora, M. Lafon, A. Casner, X. Ribeyre, K. Anderson, R. Betti, J. Delettrez, J. Frenje, V. Glebov *et al.*, Phys. Plasmas **19**, 102706 (2012).
[42]O. Klimo, V. T. Tikhonchuk, X. Ribeyre, G. Schurtz, C. Riconda, S. Weber, and J. Limpouch, Phys. Plasmas **18**, 082709 (2011).
[43]B. Yaakobi, P.-Y. Chang, A. Solodov, C. Stoeckl, D. Edgell, S. Craxton, S. Hu, J. Myatt, F. Marshall, W. Seka *et al.*, Phys. Plasmas **19**, 012704 (2012).
[44]A. A. Solodov, M. J. Rosenberg, W. Seka, J. F. Myatt, M. Hohenberger, R. Epstein, C. Stoeckl, R. W. Short, S. P. Regan, P. Michel, T. Chapman *et al.*, "Hot-electron generation at direct-drive ignition-relevant plasma conditions at the National Ignition Facility," Phys. Plasmas **27**, 052706 (2020).
[45]E. Moses and C. Wuest, "The National Ignition Facility: Status and plans for laser fusion and high-energy-density experimental studies," Fusion Sci. Technol. **43**, 420–427 (2003).
[46]S. Baton, A. Colatis, C. Rousseaux, G. Boutoux, S. Brygoo, L. Jacquet, M. Koenig, D. Batani, A. Casner, E. L. Bel *et al.*, High Energy Density Phys. **36**, 100796 (2020).
[47]M. Touati, J.-L. Feugeas, P. Nicolai, J. J. Santos, L. Gremillet, and V. T. Tikhonchuk, New J. Phys. **16**, 073014 (2014).
[48]R. M. More, in *Proceedings of 29th St. Andrews Scottish Universities Summer School in Physics Fife, Scotland* (SUSSP Publications, Edinburgh, 1985).
[49]J. D. Jackson, *Classical Electrodynamics* (Wiley, New York, 1975).